Available online at www.sciencedirect.com
ScienceDirect
Optics Communications 281 (2008) 331–340
OPTICS COMMUNICATIONS
www.elsevier.com/locate/optcom

# Anisotropic nonlinear optical absorption of gold nanorods in a silica matrix

Jean-Michel Lamarre [a,b], Franck Billard [b], Chahineze Harkati Kerboua [c], Michel Lequime [b], Sjoerd Roorda [c], Ludvik Martinu [a,*]

[a] Department of Engineering Physics, École Polytechnique de Montréal, C.P. 6079, succ. Centre-Ville, Montréal, Québec, Canada H3C 3A7
[b] Institut Fresnel, UMR CNRS 6133, Université Paul-Cézanne Aix-Marseille III, 13397 Cedex 20, Marseille, France
[c] Physics Department, Université de Montréal, C.P. 6128, succ. Centre-Ville, Montréal, Québec, Canada H3C 3J7

Received 15 May 2007; received in revised form 20 August 2007; accepted 10 September 2007

**Abstract**

Nanocomposite films consisting of gold nanospheres or gold nanorods embedded in a silica matrix have been prepared using a hybrid deposition technique consisting of plasma-enhanced chemical vapor deposition of $SiO_2$ and co-sputtering of gold, followed by annealing at 900 °C. Subsequent irradiation with 30 MeV heavy ions ($Cu^{5+}$) was used to form gold nanorods. Linear and nonlinear optical properties of this material are closely related with the surface plasmon resonance in the visible. The nonlinear absorption coefficient ($\alpha_2$@532 nm) for the films containing gold nanospheres was measured by Z-scan and P-scan techniques, and it was found to be isotropic and equal to $-4.8\times10^{-2}$ cm/W. On the contrary, gold nanorods films exhibited two distinct surface plasmon resonance absorption bands giving rise to a strong anisotropic behavior, namely a polarization-dependent linear absorption and saturable absorption. Z-scan and P-scan measurements using various light polarization directions yielded nonlinear absorption coefficient ($\alpha_2$@532 nm) values varying from $-0.9\times10^{-2}$ cm/W up to $-3.0\times10^{-2}$ cm/W. Linearity of the P-scan method in the context of nanocomposite saturable absorption is also discussed.


*PACS:* 42.65.−k; 72.80.Tm

*Keywords:* Nanocomposite; Nonlinear optics; Anisotropic optical properties; Gold nanorods

## 1. Introduction

For more than a century, there has been a considerable interest in metal/dielectric nanocomposite (NC) materials [1,2]. Indeed, NC often exhibit some characteristic properties that significantly exceed those of the individual components. NC consisting of gold nanoparticles embedded in a silica matrix lead to surface plasmon resonance (SPR) giving rise to an important absorption band in the visible. For wavelengths near the SPR, the local electromagnetic field inside the particles is enhanced leading to a strong amplification of the third order nonlinear optical (NLO) properties of the NC as first reported by Ricard et al. [3]. According to this model, for small metal volume concentration $p$, the NC third order susceptibility $\chi^{(3)}$ is a function of the metal concentration, the bulk metal third order susceptibility $\chi^{(3)}_m$, the local field factor $f(\omega)$ and the incident light angular frequency $\omega$ as related by the following equation:

$$\chi^{(3)} = pf(\omega)^2|f(\omega)|^2\chi^{(3)}_m. \quad (1)$$

For independent spherical particles, the local field factor is defined by

$$f(\omega) = \frac{3\epsilon_d}{\epsilon_m + 2\epsilon_d}, \quad (2)$$

* Corresponding author. Tel.: +1 514 340 4099.
*E-mail address:* ludvik.martinu@polymtl.ca (L. Martinu).

0030-4018/$ - see front matter © 2007 Elsevier B.V. All rights reserved.
doi:10.1016/j.optcom.2007.09.018

where $\epsilon_m$ and $\epsilon_d$ are, respectively, the metal and matrix dielectric permittivities. It turns out that the NLO properties of NC materials are strongly dependent on the nanostructure of the films. Indeed, the metal dielectric permittivity is strongly correlated with the SPR spectral position that in turn depends on the particle size and shape. Therefore, in order to fabricate high performance NLO NC, a high number of structural parameters needs to be precisely controlled.

Gold nanoparticles and NC have been fabricated by different techniques including sputtering [4–10], sol–gel [11], ion implantation [12,13], colloidal or chemical preparations [3,14–16], hybrid techniques combining, for example, plasma-enhanced chemical vapor deposition (PECVD) and sputtering [17–19] and other methods [20–23]. For reviews, see [24,25].

In previous papers [26,27], we reported on the relationship between the tailored microstructure and the linear optical properties of $Au/SiO_2$ films prepared by a hybrid technique based on PECVD and pulsed-DC sputtering. Further high temperature annealing allows gold nanoparticle size control, while subsequent heavy ion beam irradiation allows particle shape modification. The advantage of this approach, based on the work of Dalacu et al. [17–19] and Roorda et al. [28], is to allow the production of so-called aligned gold nanorods (GNR) embedded in a silica matrix. Thus, since all the rods' long axes are aligned as a consequence of the fabrication process, the material is highly anisotropic. This property gives rise to an interesting feature: the film linear optical properties are different whether they are measured along the nanorods long or short axes. We believe that the NLO properties should follow the same behavior since the local field factor (as in Eqs. (1) and (2)) is a function of the linear optical properties. Since the third order nonlinearity depends on the fourth power of the local field factor, one would expect that the anisotropy effect may even be more significant. Consequently, our objective is to measure the anisotropic NLO absorption of gold GNR films and to compare GNR results with measurements performed on films containing gold nanospheres (GNS).

In general, the NLO properties of isotropic gold NC have been measured by degenerate four wave mixing (DFWM) [3,6–9,12] and Z-scan techniques [4,5,10,11,13,15,21–23]. Z-scan tends to be the preferred method since it offers the possibility to determine both the sign and the magnitude of the real and the imaginary parts of the third order dielectric susceptibility and it is easier to implement. Also, the measurement does not require the use of a reference sample, and it is sensitive to all contributions (both thermal and electronic) to the nonlinear absorption.

First reports on NLO properties of gold nanorods [14] as well as studies dealing directly with saturable absorption of metal/dielectric NC [14,29–31] were recently published. To our knowledge, a study on silver nanorods by Kyoung et al. [32] is the only paper that touches on the topic of experimental measurements of anisotropic third order NLO properties of metal nanorods. The lack of work reporting on this subject may be explained by the relative difficulty to produce films or samples with nanorods aligned in a uniform direction. Indeed, typical nanorods preparation methods include colloidal and chemical techniques that produce randomly oriented nanorods and hence no macroscopic anisotropy. Only few papers deal with materials with anisotropic NLO properties. Among them, a recent article by Rozhin et al. presents detailed results on anisotropic saturable absorption in single-wall carbon nanotubes [33]. Also, polarization-dependent second order optical effects have been reported in gold nanoarrays by Canfield et al. [20] and McMahon et al. [34].

The next sections of the paper are organized as follows: In Section 2, we will describe the film fabrication process. Section 3 will deal with the physical origin of gold NC nonlinear absorption, while in Section 4 theory behind the Z-scan and P-scan techniques and their methodology will be discussed. Section 5 consists of the results obtained for the linear and NLO properties of GNS and GNR. Finally, general discussion of our results and analysis of the linearity of the P-scan technique are presented in Section 6.

## 2. Film fabrication

A detailed description of the GNS and GNR films can be found elsewhere [26,27]. First, spherical gold particles are deposited into a $SiO_2$ matrix by a hybrid process combining PECVD with $SiH_4$ and $O_2$ chemistry and pulsed-DC sputtering of gold. Samples are then annealed at 900 °C for a few hours in order to promote the particles growth up to a mean size of around 20 nm. At this point, we obtained a so-called GNS sample. The samples were finally exposed to a 30 MeV $Cu^{5+}$ ion beam with a 45° incidence angle (see Fig. 1). The exposure to the ion beam deformed the spherical particles (GNS) into nanorod-like structure as shown schematically in Fig. 1. Gold volume concentration for the samples described in this study is about 20%, while sample thickness is between 150 and 300 nm as evaluated by TEM, ellipsometry and Rutherford Backscattering (RBS).

TEM images of irradiated and non-irradiated regions are shown in Fig. 2. In both images, gold particles appear

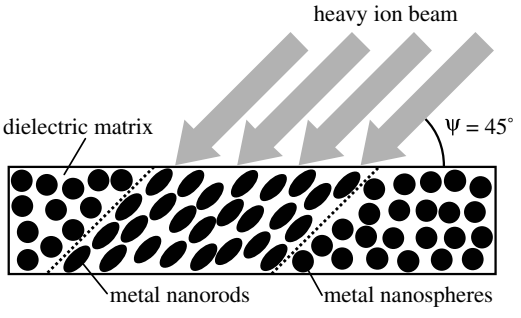


Fig. 1. Schematic representation of a cross-section of the sample modification by ion beam irradiation at a $\Psi = 45°$ angle. Spherical particles are deformed into rod-like particles with long-axis aligned with the ion beam direction.

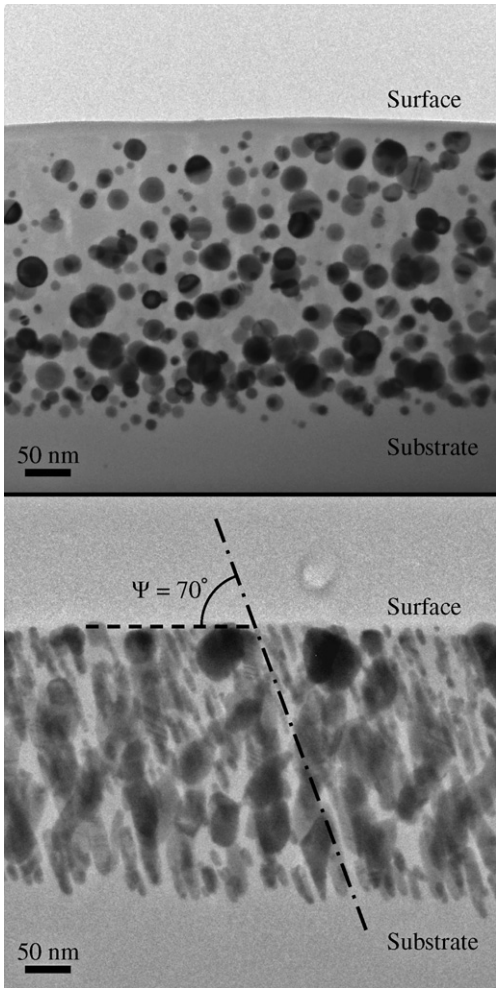


Fig. 2. Cross-section bright field TEM pictures of gold nanocomposite samples. Top: Annealed non-irradiated sample showing isotropic spherical particles. Bottom: Irradiated with $10^{15}$ ions/cm$^2$ at $\Psi = 70°$ from the sample surface. Spherical particles are deformed into rod-like particles with long-axis aligned with the ion beam direction shown by the dotted-dashed line.

dark while the $SiO_2$ matrix appears gray. In the annealed non-irradiated sample, the particles are clearly spherical with a size up to about 30 nm. The bottom part of the figure shows a region that was irradiated using an angle $\Psi = 70°$. In the irradiated region, small particles are deformed into nanorods aligned along the ion beam direction. However, large particles seem rather undeformed with a maximum size close to 50 nm, indicating probable coalescence during the irradiation step. Coalescence effect is in accordance with our previous results [26]. Lack of deformation of large particles is the subject of undergoing studies on the deformation mechanism of gold nanoparticles (see, for example [35]).

## 3. Origins of nonlinear response in gold nanocomposites

Gold/silica nanocomposites with particle size in the nanometer range exhibit intensity-dependent absorption which can be described in terms of linear and nonlinear absorption coefficients

$$\alpha = \alpha_0 + \alpha_2 I + \alpha_4 I^2 \cdots, \tag{3}$$

where $\alpha_0$, $\alpha_n$ and $I$ are, respectively, the linear absorption coefficient, the $(n+1)$th order nonlinear absorption coefficient and the intensity at the considered point. The origin of the nonlinearity of gold NC is rather complex. Even if one uses effective medium theories to simplify the problem, such as in Eqs. (1) and (2), for example, predicting the NC optical nonlinearities still involves complete calculation of the local field factor and the knowledge of the bulk gold nonlinear properties.

Bulk gold nonlinearity is relatively well understood. Detailed explanation of the nature of the nonlinear response of gold is presented by Qu et al. [21]. In the model developed by Hache et al. [36], the nonlinear susceptibility of gold is mainly imaginary and it arises from 3 different contributions: (i) intraband transitions between filled and empty states of the sp conduction bands [36,37], (ii) interband transitions between the d-bands and sp bands, and (iii) formation of hot electrons. More details on gold band structure may be found in Refs. [38,39].

Intraband, interband and hot electron contributions are of electronic nature and induce a nonlinear polarization term leading to a nonlinear absorption effect. These aforementioned mechanisms are fast (few hundreds femtoseconds or less). Additional slower mechanisms [36,40,41] such as thermal accumulation and mechanical effects (e.g. electrostriction) may add a significant contribution to the third order nonlinearity. These effects have typically a relatively long response time compared to electronic effects. For example, thermal accumulation in glass has a response time of the order of milliseconds. The nonlinear absorption coefficient measured using nanosecond pulse length can be affected by thermal effects. In our experimental conditions, low repetition rates of the laser source are used to minimize such effects. More discussion of the thermal contribution to the nonlinear third order susceptibility of gold NC can be found elsewhere [36,42,43].

## 4. Third-order nonlinear optical characterization by Z-scan and P-scan techniques

In Z-scan experiment, the transmission of a sample is measured as a function of its position along the axis of propagation of the laser beam (the $z$-axis). The results are processed in order to evaluate the nonlinear absorption coefficient. A model to describe the nonlinear absorption of a thin sample probed with a moderate intensity Gaussian beam has been proposed by Sheik-Bahae et al. [44]:

$$T(z) = \sum_{m=0}^{\infty} \left[ \frac{-\alpha_2 I_0 L_{\text{eff}}}{1 + (z/z_0)^2} \right]^m \times (m+1)^{-3/2}. \tag{4}$$

In this equation, $z_0$ is the Rayleigh range of the Gaussian beam and $I_0$ is the on-axis intensity at the beam waist

($z = 0$). One should note that Eq. (4) is valid only for $|\alpha_2 I_0 L_{\text{eff}}| \leqslant 1$ or else the series diverges. The effective length $L_{\text{eff}}$ is used to correct for the intensity decrease along the depth of the sample due to linear absorption:

$$L_{\text{eff}} = \frac{1 - e^{-\alpha_0 L}}{\alpha_0}. \tag{5}$$

For weak linear absorption, $L_{\text{eff}}$ may be replaced by the physical sample thickness $L$. This correction does not take into account the variation of intensity caused by the nonlinear absorption itself (for more discussion, see Section 6.2).

Nonlinear absorption can also be probed using an alternative technique named P-scan during which the incident power is directly varied and the induced changes in the sample transmission are measured. For small nonlinear effects, the absorption coefficients expansion (Eq. (3)) can be reduced to the first two terms, $\alpha_0 + \alpha_2 I$. The transmission factor $T$ of the sample can then be expressed as a function of intensity using the standard Beer–Lambert law:

$$T = Ce^{-\alpha L} = Ce^{-(\alpha_0 + \alpha_2 I)L}, \tag{6}$$

where $C$ is a constant. If the factor $|\alpha_2 I_0 L_{\text{eff}}|$ is small compared to unity, it is possible to approximate the transmission with the following expression:

$$T(I) \approx T(0) - T(I) L_{\text{eff}} \alpha_2 I, \tag{7}$$

where $T(0)$ is a constant depending on $C$ and on the linear transmission $e^{-\alpha_0 L}$. The beam on-axis intensity is expressed as a function of the pulse power $P_{\text{m}}$ measured before the sample:

$$I = \frac{(1 - R)P_{\text{m}}}{\pi \omega_0^2}. \tag{8}$$

Here, $R$ is the sample front interface reflection coefficient and $\omega_0$ is the beam radius (@1/e in intensity) at the considered position (usually the beam waist). Thus, the transmission can be calculated as a function of the measured power as

$$T(P_{\text{m}}) \approx T(0) - T(0) L_{\text{eff}} \alpha_2 \frac{1 - R}{\pi \omega_0^2} P_{\text{m}}, \tag{9}$$

indicating a linear dependence between the measured power and the sample transmission. It is possible to extract $\alpha_2$ from the slope of the $T(P_{\text{m}})$ vs. $P_{\text{m}}$ dependance (or $T(I)$ vs. $I$).

The experimental setup used in this work is schematically shown in Fig. 3. Z-scan and P-scan measurements were performed using a Q-switched Nd-YAG laser emitting at 1064 nm. Laser pulses were converted in second harmonic pulses resulting in the final 532 nm wavelength. A low wavelength pass filter was used to remove any remaining power at 1064 nm. The total pulse length was 22 ns as measured with a fast pin-photodiode linked to an oscilloscope. The pulse length measurement system had a total bandwidth of 500 MHz. The sample measurements were performed using a 10 Hz repetition rate in order to minimize the nonlinear thermal effect and sample damaging. The laser beam was spatially-filtered and focused by a 100 mm focal lens to obtain a beam radius of 16.8 μm at the beam waist. The beam profile was measured using a CCD camera. The intensity range used was between several MW/m$^2$ and 5 GW/m$^2$. These values were calculated from pyrometer energy measurements, the beam area at the waist and the pulse length. The choice of the maximum power value is important to assure the linearity of the method (as it will be discussed in Section 6.2). The laser beam was separated into a reference arm and a sample measurement arm using a silica wedge. A wedge was used instead of a beam splitter in other to avoid interferences in the focal volume. The intensities of the reference and signal beams were measured using standard photodiodes linked to a digital oscilloscope with a reduced 20 MHz bandwidth. Special attention was taken to set-up reference and signal arms as similar as possible. Thus, optical paths of the reference line and the sample line were kept close to each other in order to minimize the measurement delay between pulses. Furthermore, incoming powers were set at similar values in order to obtain as identical photodiode responses as possible. Finally, the sample was mounted on a motorized translation stage.

The P-scan configuration offers at least two advantages over the traditional Z-scan measurements, namely it is less

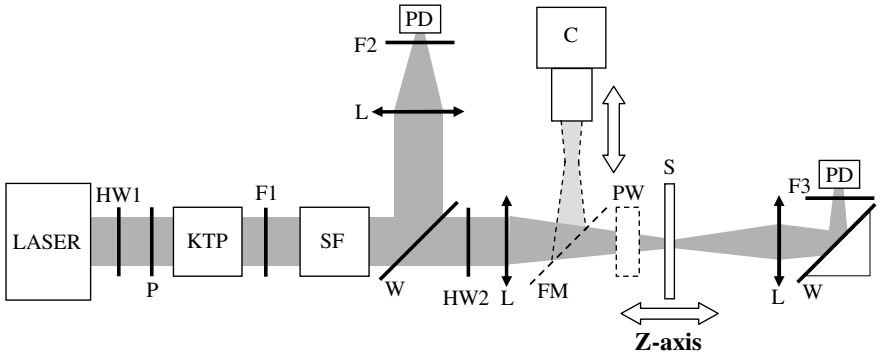


Fig. 3. Experimental setup for P-scan and Z-scan measurements. Laser. HW1: half-wave plate (1064 nm). P: polarizer, KTP frequency doubling crystal. F1: absorbing filter for 1064 nm, SF: spatial filter, W: wedge, L: lenses, F2 and F3: attenuators, FM: mirror on a flip mount, C: camera mounted on translation axis, HW2: half-wave plate (532 nm), PW: pyrometer, S: sample mounted on a translation stage, PD: photodiode.

time consuming and is less sensitive to geometry issues (parallelism, reflections, dust, etc.). In order to realize P-scan measurements, the power per pulse was adjusted with a rotating half-wave plate (HW1) located before the polarizer. We verified that no transmission variations were observed for an empty sample P-scan measurement. We also checked that the photodiode responses were linear for the used intensity range. Lastly, polarization dependent measurements were performed by rotating the polarization plane using the half wave plate (HW2) located in the sample measurement arm.

## 5. Results and discussion

In this section, we present the optical measurements results we obtained for the GNS and GNR. Understanding the geometry of our experiment is crucial for the analysis of our results since the anisotropic nonlinear effect is a consequence of the global alignment of the nanorods long axes. An appropriate choice of light polarization direction allows one to probe the anisotropy. Fig. 4 schematically shows the light propagation direction and the polarization directions relative to the GNR long-axis alignment. Sample surface is parallel to the $x$–$y$ plane while the laser beam propagation direction is along the $z$-axis. The GNR long-axis is located in the $y$–$z$ plane and makes a 45° angle with the $y$-axis. The polarization direction of the incident beam is in the $x$–$y$ plane and makes an angle $\theta_{pol}$ with the $x$-axis. The projection along the light grey plane allows one to observe that the scalar product between the long-axis and the $x$-axis equals zero. It follows that for a polarization direction along the $x$-axis, only the GNR short-axis SPR is stimulated. Polarization along the $y$-axis direction (dark grey plane) can be separated into two components: one along the GNR short-axis and the other along the long-axis. By rotating the polarization, it is possible to change the polarization in a continuous way from the excitation of the short-axis resonance only (polarization along $x$-axis, $\theta_{pol} = 0°$) to a 50/50 excitation of the short and long axes (polarization along $y$-axis, $\theta_{pol} = 90°$).

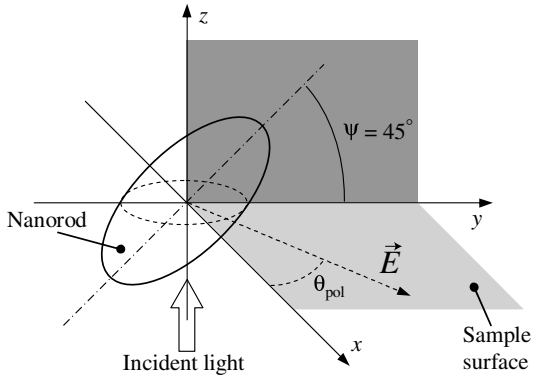


Fig. 4. Schematic representation of the polarization dependent measurements. The GNR long-axis is directed at a 45° angle for the $y$-axis in the $y$–$z$ plane. The laser beam propagation direction is along the $z$-axis, while the polarization direction is varied along the $\theta_{pol}$ angle in the $x$–$y$ plane, which corresponds to the sample surface.

### 5.1. Linear optical characteristics

The experimental results for the polarized linear optical transmission of GNS and GNR samples are shown in Fig. 5. The response from spherical particles is independent of the polarization with a maximum absorption located at 530 nm. This is not surprising considering that the material is isotropic. GNR spectra are, however, much different since they exhibit two distinct absorption bands associated with the SPR along the long and short axes of the nanoparticles. Polarization along $\theta_{pol} = 0°$ excites the short-axis SPR resonance located at 506 nm. Polarization along $\theta_{pol} = 90°$ excites both the short-axis (506 nm) and the long-axis (~575 nm) SPR leading to a broader absorption band (see Fig. 4 for the geometry).

### 5.2. Nonlinear absorption properties of gold spherical nanoparticles (GNS)

P-scan results for GNS samples are shown in Fig. 6. The data were normalized so that the transmittance at zero intensity is equal to unity (no nonlinear effect). The dependence of the normalized transmittance on the intensity is linear as indicated by the very good linear regression fit obtained as predicted by Eqs. (7) and (9). The value obtained for the nonlinear absorption coefficient is $-4.8 \pm 1.1 \times 10^{-2}$ cm/W. The error has been obtained by performing the measurement several times on different parts of the sample.

Fig. 7 presents the results of Z-scan experiments performed on the GNS sample used to produce the P-scan graph presented in Fig. 6. For this measurement, the on-axis intensity at the beam waist was 4.5 GW/m$^2$. The theoretical Z-scan curve calculated using Eq. (4) and corresponding to the nonlinear absorption coefficient obtained by P-scan measurements is also plotted. Note that other parameters used (thickness, linear absorption coefficient,

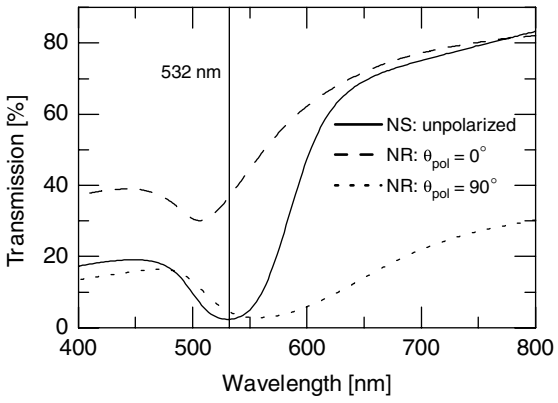


Fig. 5. Linear transmission spectra for GNS and GNR. The vertical line indicates the NLO measurement wavelength.

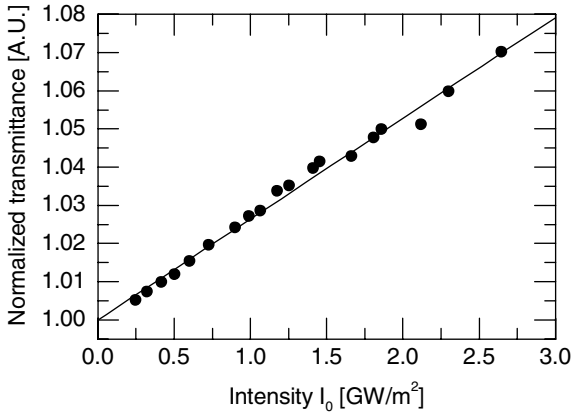


Fig. 6. P-scan measurements on GNS sample. Linear fit of the slope yielded a nonlinear absorption coefficient $\alpha_2$ of $-4.8 \pm 1.1 \times 10^{-2}$ cm/W.

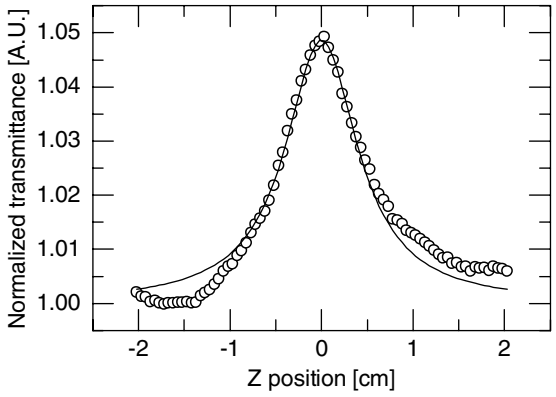


Fig. 7. Z-scan measurements on GNS samples. The value of the nonlinear coefficient used as fit-parameter (full line) is obtained from the P-scan measurements.

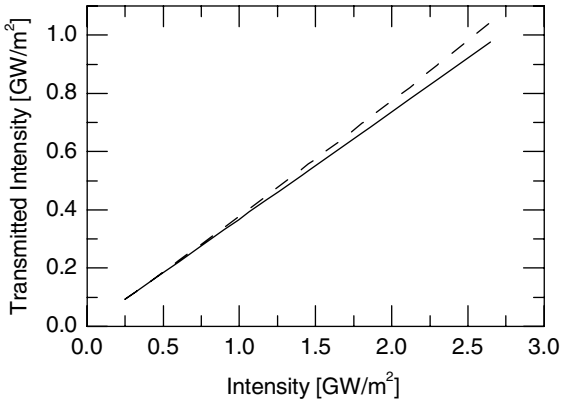


Fig. 8. Normalized transmittance of the GNS sample. Solid line – linear transmission; dashed line – nonlinear + linear transmission.

etc.) were the same as for the P-scan calculation. The agreement between the experimental data and the calculated curve is very good. The parameters of the Z-scan curve were extracted from the P-scan measurements and not fitted. P-scan and Z-scan measurements yield identical nonlinearity values. This clearly underlines the validity of our procedure and confirms the assumptions of the model: thin sample, Gaussian beam and weak nonlinearity.

In order to obtain a general idea of the importance of the nonlinear effect compared to the linear transmission, we plotted both the absolute linear and nonlinear corrected (linear + nonlinear) transmissions of the sample in Fig. 8. One can see that when the intensity becomes high enough, the change in absolute transmission is quite important especially when one considers that the sample is thin (150 nm). Even for a relatively low intensity (several GW/m$^2$), the nonlinear corrected transmission can be almost 10% higher than the linear transmission. Therefore, using a thicker sample and/or higher intensities would lead to a very strong response.

### 5.3. Nonlinear absorption properties of gold nanorods (GNR)

Polarization dependent measurements performed on GNR samples are presented in Fig. 9. The polarization angle $\theta_{pol}$ was varied between 0° and 90° by steps of 15° in order to vary the excitation ratio of the GNR long and short-axis SPRs. The data were normalized so that the transmission at zero intensity equals 1 (no nonlinear effect). For each angle, the slope was fitted in order to extract the nonlinear absorption coefficient $\alpha_2$. Fig. 10 presents the fitted nonlinear absorption coefficient as a function of $\theta_{pol}$. It can be observed that $\alpha_2$ is negative as it was the case for the GNS. Principal results obtained for GNS and GNR with $\theta_{pol} = 0°$ and $\theta_{pol} = 90°$ are reported in Table 1.

First, one should note that the nonlinear absorption coefficient is 3.3 times higher for $\theta_{pol} = 90°$ than for $\theta_{pol} = 0°$. Secondly, it is important to notice the *S*-shape

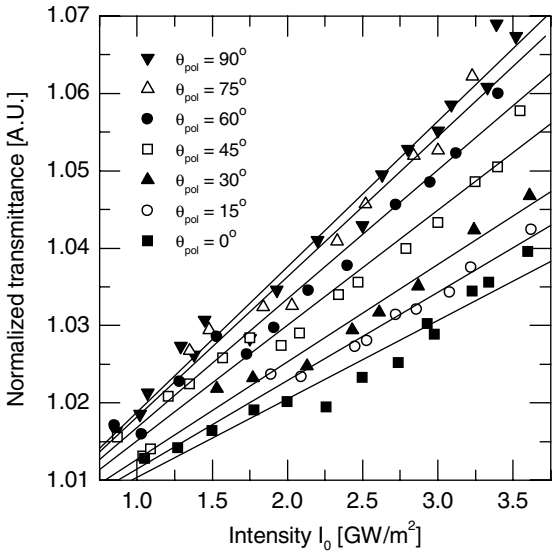


Fig. 9. P-scan measurements for GNR performed with a polarization angle $\theta_{pol}$ varying between 0° and 90° by steps of 15°. The measurements were normalized and linearly fitted to extract the nonlinear absorption coefficient $\alpha_2$.

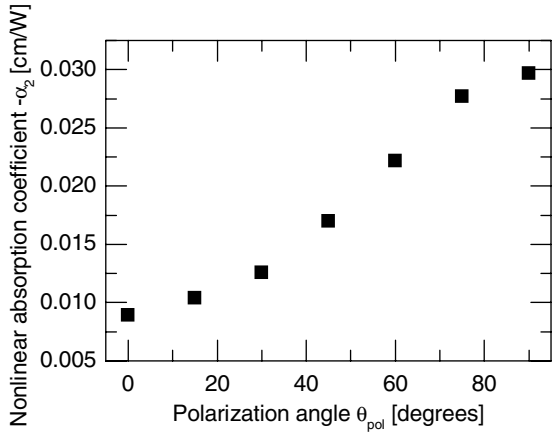


Fig. 10. Nonlinear absorption coefficient $\alpha_2$ plotted as a function of the polarization angle $\theta_{pol}$ (see Fig. 4 for the geometry).

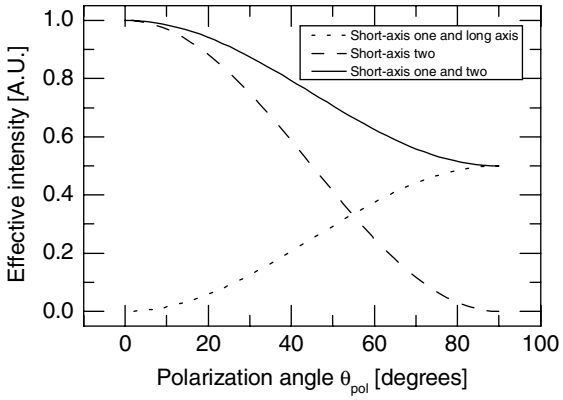


Fig. 11. Plot of the effective intensity along each principal axis of the GNR as a function of the polarization angle. Note that one short-axis and the long-axis are submitted to the same intensity profile. At $\theta_{pol} = 0°$, the whole intensity is along one short-axis while at $\theta_{pol} = 90°$ the intensity is separated equally between the second short-axis and the long-axis.

Table 1
Values measured for different sample orientations

| Sample | Nonlinear absorption coefficient (cm/W) |
|---|---|
| Gold nanospheres (GNS) | $-4.8 \times 10^{-2}$ |
| Gold nanorods (GNR), $\theta_{pol} = 90°$ | $-3.0 \times 10^{-2}$ |
| Gold nanorods (GNR), $\theta_{pol} = 0°$ | $-0.9 \times 10^{-2}$ |

of the experimental curve. In order to understand the physical reason for both those observations, one should remember that the ratio of components of the electric field along the short and long axes of the GNR vary with $\theta_{pol}$. Using appropriate projections (see Fig. 4), it is possible to calculate the effective intensity, which excites each axis SPR. These expressions are presented in Table 2 and plotted in a normalized form in Fig. 11.

The apparent nonlinear absorption coefficient for different polarization directions $\theta_{pol}$ can be expressed as follows:

$$\alpha_2(\theta_{pol}) = [f_{SA1}(\theta_{pol}) + f_{SA2}(\theta_{pol})]\alpha_2^{SA} + f_{LA}(\theta_{pol})\alpha_2^{LA}, \quad (10)$$

where $\alpha_2^{SA}$ and $\alpha_2^{LA}$ are, respectively, the short and long-axis contributions to the nonlinear absorption coefficient. At $\theta_{pol} = 0°$, the electric field is directed along the short-axis, while at $\theta_{pol} = 90°$ the electric field is separated between the short-axis and the long-axis so that the effective intensity is the same for both SPRs. Writing Eq. (10) for $\theta_{pol} = 0°$ and 90° and using the values of Table 1, we obtain:

$$\begin{aligned} &\text{For } \theta_{pol} = 0° \quad \alpha_2^{SA} = -0.9 \times 10^{-2} \text{ cm/W}. \\ &\text{For } \theta_{pol} = 90° \quad (\alpha_2^{SA} + \alpha_2^{LA})/2 = -3.0 \times 10^{-2} \text{ cm/W}. \end{aligned} \quad (11)$$

Table 2
Effective intensity factors along the GNR principal axis

| Direction | Projected intensity factor |
|---|---|
| Long axis | $f_{LA}(\theta_{pol}) = \sin^2\theta_{pol}\cos^2 45°$ |
| First short-axis | $f_{SA1}(\theta_{pol}) = \sin^2\theta_{pol}\cos^2 45°$ |
| Second short-axis | $f_{SA2}(\theta_{pol}) = \cos^2\theta_{pol}$ |

Solving these equations yields the value of $\alpha_2^{LA} = -5.1 \times 10^{-2}$ cm/W. This means that the contribution from the long-axis is 5.7 times higher than the one along the short-axis. Since the long-axis contribution is dominant, it seems normal that the long-axis intensity profile as a function of $\theta_{pol}$ follows an S-shape (Fig. 11), similar to the one observed for the nonlinear absorption coefficient of the sample (Fig. 10).

A complete explanation for the dominance of the long-axis contribution over the short-axis one is rather complex. In order to interpret the ratio of 5.7 between both contributions, a detailed analysis of the local field is needed. Also, Eqs. (1) and (2) should be modified in order to take into account the geometry of the GNR. The difference between the values obtained for GNS ($-4.8 \times 10^{-2}$ cm/W) and GNR may also be explained using the same argument. The presence of larger spherical particles in the irradiated region also plays a role in the nonlinear response. However, since those particles are isotropic, they should not contribute to the polarization dependance observed here. P-scan and Z-scan measurements with different repetition rates (5, 10, 20 Hz) showed no significant differences indicating no thermal accumulation between pulses.

## 6. General discussion

### 6.1. Comparison with published data

Comparison of the obtained results with the values published in the literature is difficult due to the difference of materials (particle size, shape, concentration and distribution) and measurement conditions (wavelength, pulse length). This leads to large differences in the nonlinearity values published for gold NC (several orders of magnitude) [3–13,15,21–23]. Similar gold/silica nanocomposites samples with spherical particle (comparable nanostructure, fabrication process and measurement parameters) were measured by Debrus et al. [4] using the Z-scan technique.

The mean particle size they obtained is 2 nm which is smaller than the particles of our study. The laser source they used (Q-switched Nd:YAG frequency doubled 532 nm, 7 ns, 10 Hz) was similar to the one in our experiment (Q-switched Nd:YAG frequency doubled 532 nm, 22 ns, 10 Hz). In the end, the value we obtained ($\alpha_2 = -4.8 \times 10^{-2}$ cm/W) is comparable to the value they obtained ($\alpha_2 = -1.1 \times 10^{-2}$ cm/W). Indeed, particle size distribution differences may easily account for the difference in the measured values.

### 6.2. Analysis of linearity of the P-scan technique

The importance of the nonlinearity observed (up to 10%, see Fig. 8) led us to consider the effect of the decrease of intensity along the depth of the sample caused by the nonlinear effect. In order to investigate the contribution of the nonlinear absorption on the variation of intensity we performed numerical simulations using three different models, the first one being the conventional correction for $L_{\text{eff}}$ presented in Eqs. (5) to (9). This model takes into account the decrease of intensity along the propagation distance in the sample due to linear absorption. The second model (NLA) corrects the intensity for linear and nonlinear absorption. In order to calculate the transmission for this model, we separated the active NC layer in $N = 20,000$ thin layers. For each layer $i$, we calculated the cumulative transmission (total transmission of layers $i, i-1, i-2 \ldots, 1, 0$) using Eq. (12) (see also Eq. (6)) in order to obtain the total transmission of the stack:

$$T_i = T_{i-1} \times e^{-\alpha \frac{L}{N}} = T_{i-1} e^{\left(-(\alpha_0 + \alpha_2 I_i)\frac{L}{N}\right)}, \tag{12}$$

where,

$$I_i = T_{i-1} I_0. \tag{13}$$

Naturally, $T_0 = 1$.

Finally, two-level saturable absorption model (SAM) [40,45] represented in Eq. (14) is the third model we simulated. This model accounts for the decrease of absorption in NC materials with a rise of intensity, as used by several authors [11,30,30,33]. According to the SAM, the absorption coefficient is given by

$$\alpha = \frac{\alpha_0}{1 + I/I_{\text{sat}}}, \tag{14}$$

where $I_{\text{sat}}$ is the saturation intensity. In the same way as for the second model, we are able to calculate the sample transmission numerically in the context of the SAM using $\alpha$ predicted by Eq. (14) in Eq. (12). The SAM can be linked to the absorption coefficient of Eq. (3) by rewriting the right part of Eq. (14) in a Taylor power series (provided that the intensity is small compared to the saturation intensity) in order to deduce the value of the nonlinear absorption coefficients:

$$\alpha \approx \alpha_0 - \frac{\alpha_0}{I_{\text{sat}}} I + \frac{\alpha_0}{I_{\text{sat}}^2} I^2 - \cdots \tag{15}$$

Comparing Eqs. (3) and (15), one can obtain the effective third order nonlinear absorption coefficient expression predicted by SAM or the value of $I_{\text{sat}}$ if one knows the values $\alpha_2$ and $\alpha_0$:

$$\alpha_2 \approx -\frac{\alpha_0}{I_{\text{sat}}}. \tag{16}$$

The simulations were performed using the parameters of the GNS sample ($L = 150$ nm, $\alpha_2 = -4.8 \times 10^{-2}$ cm/W, $\alpha_0 = 1.54 \times 10^7$ m$^{-1}$). Fig. 12 presents the simulation results for the three aforementioned models plotted in an intensity range comparable to the one used in our experiments (highest intensity used is represented by the vertical dashed line in the graph). Also plotted in Fig. 12 is the purely linear case calculated from the slope at zero intensity.

One striking observation is that all models (effective length, SAM and NLA) clearly diverge from linearity for intensities exceeding 5 GW/m$^2$ (vertical dashed line in Fig. 12). Using a linear approximation for intensities higher than the latter limit induces a minimum systematic model error of about 2%. At this value, the product $|\alpha_2 I_0 L_{\text{eff}}|$ equals 0.14 which is clearly not small compared to unity (see text between Eqs. (6) and (7)). Therefore, it would be incorrect to extract a nonlinear absorption coefficient $\alpha_2$ from a regression fit (of Eq. (7), for example) for intensity values exceeding this limit. It is also interesting to note that the NLA model diverges more rapidly from linearity than the effective length model even if it considers more precisely the absorption losses in the material. In our case, $\alpha_2$ being negative, the intensity predicted by the NLA is higher (for each sub-layer) than the one predicted by the effective length model, hence the total nonlinear effect is more important and the curve diverges towards higher transmission. SAM includes by definition (see Eqs. (14) to (16)) the contributions of higher orders

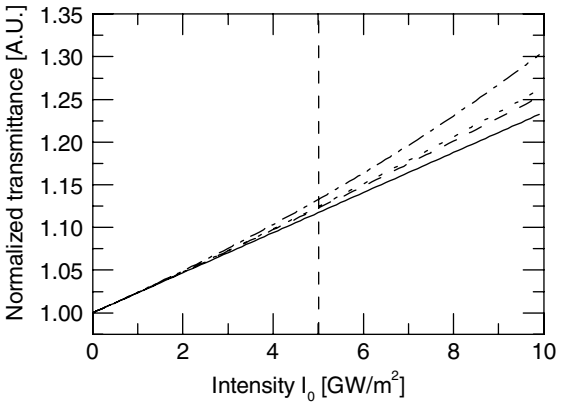


Fig. 12. Simulated P-scan curves for different models. Dashed line – absorption saturation model (SAM); solid line – linear model calculated from the derivative of the intensity saturation model for zero intensity; dotted line – simple model with correction for linear absorption ($L_{\text{eff}}$); dashed/dotted line – simple model with correction for linear and nonlinear absorption (NLA). Vertical dashed line indicates the maximum value of intensity used in our measurements.

$(\alpha_4, \alpha_6, \ldots)$. It is therefore normal that the model ceases to be linear at higher intensity. If one is to consider the SAM as physically valid, it follows that it is not appropriate to give values of $\alpha_2$ alone for an intensity exceeding the linearity limit (5 GW/m$^2$ for our sample). In that case, one must either consider higher order effects or simply use the $I_{sat}$ parameter. Interestingly, our simulation also shows that using the effective length model in the nonlinear part of the graph (intensity higher than 5 GW/m$^2$) yields results closer to the SAM and the linear approximation than the NLA, even if the effective length model represents a least complete description.

## 7. Conclusions

We have fabricated gold/silica nanocomposites consisting of gold spheres (GNS) or nanorods (GNR) embedded in a silica matrix. GNS exhibited a high saturable absorption with a value of $\alpha_2 = -4.8 \times 10^{-2}$ cm/W comparable to the results published in the literature. GNR samples were fabricated such that all particles long axes were aligned along the path of the ion beam irradiation. These samples exhibited a highly anisotropic saturable absorption varying between $\alpha_2 = -0.9 \times 10^{-2}$ and $-3.0 \times 10^{-2}$ cm/W due to splitting of the spherical particle SPR into short-axis and long-axis SPR. Variation in the contribution of each axis as a function of the polarization angle is an important parameter that dictates the magnitude of the nonlinear response. We found the long-axis and short-axis contributions to attain, respectively, $-5.1 \times 10^{-2}$ cm/W and $-0.9 \times 10^{-2}$ cm/W. We also investigated the linearity of the P-scan measurement. Our results show, in the context of our samples, that the linear approximation is valid up to a higher intensity limit of 5 GW/m$^2$. We showed that the use of the $L_{eff}$ correction is surprisingly more robust than the NLA model even if one exceeds slightly the intensity limit.

Further experimentations should include the measurement of the nonlinear absorption coefficient as a function of wavelength in order to probe the spectral dependence of the nonlinearity for both short-axis and long-axis polarizations. Correlation with a measurement of the local field factor by others means (such as obtaining the anisotropic dielectric constants by ellipsometry) would also be of interest. Fabrication of samples with smaller irradiation angles (see Fig. 3) would allow one to probe more easily the long-axis/short-axis contributions by augmenting the anisotropic ratio (keeping the same polarization configuration). Similarly, a higher irradiation angle would give a lower anisotropy. Hence, one can obtain a tunable anisotropy by controlling the irradiation angle.

## Acknowledgements

The authors wish to thank Mr. Francis Turcot for his technical assistance with the deposition process and they also gratefully acknowledge valuable discussions with Pr. H. Akhouayri of the Institut Fresnel in Marseille. This work was supported by FQRNT (Québec) and NSERC (Canada). J.-M. Lamarre acknowledges the FQRNT and NSERC scholarships and the France-Québec exchange program.

## References

[1] J.C. Maxwell-Garnett, Philos. Trans. Roy. Soc. Lond. A 203 (1904) 385.
[2] J.C. Maxwell-Garnett, Philos. Trans. Roy. Soc. Lond. A 205 (1906) 237.
[3] D. Ricard, P. Roussignol, C. Flytzanis, Opt. Lett. 10 (1985) 511.
[4] S. Debrus, J. Lafait, M. May, N. Pinçon, D. Prot, C. Sella, J. Venturini, J. Appl. Phys. 88 (2000) 4469.
[5] N. Pinçon, B. Palpant, D. Prot, E. Charron, S. Debrus, Eur. Phys. J. D19 (2002) 395.
[6] H.B. Liao, W. Lu, W. Wen, G.K.L. Wong, J. Opt. Soc. Am. B22 (2005) 1923.
[7] H.B. Liao, W. Wen, G.K.L. Wong, J. Appl. Phys. 93 (2003) 4485.
[8] H.B. Liao, R.F. Xiao, H. Wang, K.S. Wong, G.K.L. Wong, Appl. Phys. Lett. 72 (1998) 1817.
[9] I. Tanahashi, Y. Manabe, T. Tohda, S. Sasaki, A. Nakamura, J. Appl. Phys. 79 (1996) 1244.
[10] D.J. Chen, S. Ding, J.B. Han, H.J. Zhou, S. Xiao, G.G. Xiong, Q.Q. Wang, Chin. Phys. Lett. 22 (2005) 2286.
[11] M. Kyoung, M. Lee, Bull. Korean Chem. Soc. 21 (2000) 26.
[12] K. Fukumi, A. Chayahara, K. Kadono, T. Sakaguchi, Y. Horino, M. Miya, K. Fujii, K. Hayakawa, M. Satou, J. Appl. Phys. 75 (1994) 3075.
[13] E. Cattaruzza, G. Battaglin, P. Calvelli, F. Gonella, G. Mattei, C. Maurizio, P. Mazzoldi, S. Padovani, R. Polloni, C. Sada, B. Scremin, F. D'Acapito, Comp. Sci. Technol. 63 (2003) 1203.
[14] H.I. Elim, J. Yang, J.Y. Lee, J. Mi, W. Ji, Appl. Phys. Lett. 88 (2006) 083107.
[15] S. Qu, C. Du, Y. Song, Y. Wang, Y. Gao, S. Liu, Y. Li, D. Zhu, Chem. Phys. Lett. 356 (2002) 403.
[16] L. François, M. Mostafavi, J. Belloni, J.-F. Delouis, J. Delaire, P. Feneyrou, J. Phys. Chem. B 104 (2000) 6133.
[17] D. Dalacu, L. Martinu, J. Opt. Soc. Am. B18 (2001) 85.
[18] D. Dalacu, L. Martinu, Appl. Phys. Lett. 77 (2000) 4283.
[19] D. Dalacu, L. Martinu, J. Appl. Phys. 87 (2000) 228.
[20] B.K. Canfield, S. Kujula, K. Jefimovs, T. Vallius, J. Turunen, M. Kauranen, J. Opt. A: Pure Appl. Opt. 7 (2005) S110.
[21] S. Qu, Y. Zhang, H. Li, J. Qiu, C. Zhu, Opt. Mater. 28 (2006) 259.
[22] S. Qu, C. Zhao, X. Jiang, G. Fang, Y. Gao, H. Zeng, Y. Song, J. Qui, C. Zhu, K. Hirao, Chem. Phys. Lett. 368 (2003) 352.
[23] H. Shen, B. Cheng, G. Lu, W. Wang, D. Guan, Z. Chen, G. Yang, Chin. Phys. 14 (2005) 1915.
[24] H. Biederman, L. Martinu, Plasma polymer–metal composite films, in: R. d'Agostino (Ed.), Plasma Deposition, Treatment and Etching of Polymers, Academic Press, Boston, 1990, p. 269.
[25] U. Kreibig, M. Vollmer, Optical Properties of Metal Clusters, Springer, Berlin, 1995.
[26] J.-M. Lamarre, Z. Yu, C. Harkati, S. Roorda, L. Martinu, Thin Solid Films 479 (2005) 232.
[27] J.-M. Lamarre, L. Martinu, in, Proc. of the 47th Ann. Tech. Conf. of the Society of Vacuum Coaters, Dallas, SVC, 2004. p. 343.
[28] S. Roorda, T.V. Dillen, A. Polman, C. Graf, A. van Blaaderen, B.J. Kooi, Adv. Mater. 16 (2004) 235.
[29] Y. Gao, X. Zhang, Y. Li, H. Liu, Y. Wang, Q. Chang, W. Jiao, Y. Song, Opt. Commun. 251 (2005) 429.
[30] R.A. Ganeev, A.I. Ryasnyansky, A.L. Stepanov, T. Usmanov, Opt. Quantum Elect. 36 (2004) 949.
[31] R.A. Ganeev, A.I. Ryasnyansky, A.L. Stepanov, T. Usmanov, Phys. Stat. Sol. B 241 (2004) R1.

[32] M. Kyoung, M. Lee, Opt. Commun. 171 (1999) 145.
[33] A.G. Rozhin, Y. Sakakibara, H. Kataura, S. Matsuzaki, K. Ishida, Y. Achiba, M. Tokumoto, Chem. Phys. Lett. 405 (2005) 288.
[34] M.D. McMahon, R. Lopez, R.F. Haglund, E.A. Ray, P.H. Bunton, Phys. Rev. B 73 (2006) 041401.
[35] C. Harkati Kerboua, J.-M. Lamarre, L. Martinu, S. Roorda, Nucl. Instr. Meth. B 257 (2007) 42.
[36] F. Hache, D. Ricard, C. Flytzanis, U. Kreibig, Appl. Phys. A 47 (1988) 347.
[37] L. Yang, D.H. Osborne, R.F. Haglund, R.H. Magruder, C.W. White, R.A. Zuhr, H. Hosono, Appl. Phys. A 62 (1996) 403.
[38] N.E. Christensen, B.O. Seraphin, Phys. Rev. B 4 (1971) 3321.
[39] N.E. Christensen, Phys. Rev. B 13 (1976) 2698.
[40] R.W. Boyd, Nonlinear Optics, Academic Press, 1992.
[41] M. Sheik-Bahae, M.P. Hasselbeck, OSA Handbook of Optics, vol. IV, OSA, 2000 (Chapter 17).
[42] N. Del Fatti, F. Vallée, Appl. Phys. B 73 (2001) 383.
[43] M. Falconieri, J. Opt. A: Pure Appl. Opt. 1 (1990) 662.
[44] M. Sheik-Bahae, A.A. Said, T.H. Wei, D.J. Hagan, E.W.V. Stryland, IEEE J. Quant. Elec. 26 (1990) 760.
[45] P.N. Butcher, The Elements of Nonlinear Optics, Cambridge University Press, 1990.